Chemical Engineering Journal vol 442, part 2, p. 136209, 2022
https://doi.org/10.1016/j.cej.2022.136209

Enhanced CO_2 conversion on highly-strained and oxygen-deficient $BiVO_4$ photocatalyst

Saeid Akrami[1], Yasushi Murakami[2], Monotori Watanabe[3], Tatsumi Ishihara[2,3], Makoto Arita[4], Qixin Guo[5], Masayoshi Fuji[1,6,*] and Kaveh Edalati[3,*]

[1] Department of Life Science and Applied Chemistry, Nagoya Institute of Technology, Tajimi 507-0071, Japan
[2] Department of Applied Chemistry, Faculty of Engineering, Kyushu University, Fukuoka 819-0395, Japan
[3] WPI, International Institute for Carbon-Neutral Energy Research (WPI-I2CNER), Kyushu University, Fukuoka 819-0395, Japan
[4] Department of Materials Science and Engineering, Faculty of Engineering, Kyushu University, Fukuoka 819-0395, Japan
[5] Department of Electrical and Electronic Engineering, Synchrotron Light Application Center, Saga University, Saga 840-8502, Japan
[6] Advanced Ceramics Research Center, Nagoya Institute of Technology, Tajimi 507-0071, Japan

Abstract

Bismuth vanadate ($BiVO_4$) has recently received significant attention for photocatalytic CO_2 conversion due to its low bandgap and high stability, but low position of the conduction band and high electron-hole recombination rate limit its photocatalytic activity. In this study, to overcome the drawbacks of $BiVO_4$, oxygen vacancies and lattice strain are simultaneously introduced in this oxide using a high-pressure torsion process. The processed material not only shows the low recombination rate and enhanced conduction band level but also exhibits bandgap narrowing. The oxygen-deficient and highly-strained $BiVO_4$ shows a high photocatalytic CO_2 conversion rate with an activity comparable to the P25 TiO_2 photocatalyst. The enhancement of photocatalytic activity is discussed based on the modification of band structure, enhanced light absorbance, the lifetime of excited electrons, and the role of oxygen vacancies as activation sites for CO_2 photoreduction. This work introduces a feasible pathway to develop active photocatalysts for CO_2 conversion by lattice strain and defect engineering.

Keywords: Bismuth vanadate salt, Photocatalyst; Strain engineering; Defect engineering, Photocatalytic CO_2 conversion.

*Corresponding authors:
Kaveh Edalati (E-mail: kaveh.edalati@kyudai.jp; Tel: +81-92-802-6744)
Masayoshi Fuji (E-mail: fuji@ fuji@nitech.ac.jp; Tel: +81-57-227-6811)

1. Introduction

The high concentration of CO_2 in the Earth's atmosphere and consequently global warming is perhaps the most critical crisis of the 21st century [1]. Capturing CO_2 and its conversion to other useful products has received significant attention in recent years [1]. Photocatalysis using a light-absorbing catalyst such as TiO_2, C_3N_4 and $BiVO_4$ under sunlight is the cleanest technology to convert CO_2 to other useful chemicals [2,3]. During the photocatalytic CO_2 conversion, the electrons in the valence band of the photocatalyst absorb the light and transfer to the conduction band. These excited electrons and corresponding holes take part in various reactions to convert CO_2 to other products such as CO, HCOOH, HCHO, CH_3OH and CH_4 through the redox reactions with the chemical potentials given in Table. 1 [4,5]. Despite high scientific interest in photocatalytic CO_2 conversion, enhancement of the efficiency of the method is a significant challenge [2,3].

Table 1. Reactions in CO_2 conversion with their chemical potentials [4,5].

Reaction	Standard Potential (eV)
$CO_2 + 2H^+ + 2e^- \rightarrow HCOOH$	-4.20
$CO_2 + 2H^+ + 2e^- \rightarrow CO + H_2O$	-4.29
$CO_2 + 4H^+ + 4e^- \rightarrow HCHO + H_2O$	-4.33
$CO_2 + 6H^+ + 6e^- \rightarrow CH_3OH + H_2O$	-4.43
$CO_2 + 8H^+ + 8e^- \rightarrow CH_4 + 2H_2O$	-4.57

Various strategies have been used to improve the photocatalytic CO_2 conversion efficiency such as introducing heterojunctions [6], defect engineering [7,8], doping [9], strain engineering [10-12] and formation of mesoporous structures [13]. These strategies are employed to control various features of photocatalysis such as enhancing the CO_2 adsorption, increasing the light absorbance, facilitating the electron-hole separation, minimizing the electron-hole recombination, and optimizing the electronic band structure [2,14]. Defect engineering is a strategy that can affect most of the mentioned features of photocatalysis, and among different defects, oxygen vacancies are the most effective ones [7,8]. Oxygen vacancies on the surface of catalysts can act as active sites for CO_2 adsorption and electron-hole separation [7]. Moreover, it is believed that the adsorbed CO_2 on oxygen vacancies is more active for conversion due to a reduction in the binding energy of carbon and oxygen atoms [7,8]. Strain engineering via lattice compression or expansion can also reduce the overall energy barrier for the rate-controlling step of photocatalytic CO_2 conversion, either by increasing the light absorbance, aligning the band structure or by electron-hole separation [10-12]. Simultaneous engineering the defects and lattice strain without the addition of impurity atoms can be an effective solution to enhance the efficiency because impurity-induced recombination can be minimized in this way [15].

Among various photocatalysts developed for photocatalytic CO_2 conversion, $BiVO_4$ (as a mixed-metal oxide or salt) has recently received significant attention due to its high stability and low direct bandgap (2.4-2.5 eV) [16,17]. The main drawbacks of $BiVO_4$ which limit its photocatalytic CO_2 conversion efficiency are its low conduction band energy level and high rate of electron and hole recombination [17,18]. To improve the photocatalytic CO_2 conversion on $BiVO_4$, most reported studies introduced heterojunctions as a strategy: $BiVO_4/C_4N_3$ [18], $BiVO_4\{010\}/Au/Cu_2O$ [19], $BiVO_4/C/Cu_2O$ [20], $ZnIn_2S_4/BiVO_4$ [21], $BiVO_4/Bi_4Ti_3O_{12}$ [22], and $Cd_xZn_{1-x}S@Au/BiVO_4$ [23]. Doping with other elements such as Bi, Cu and Ag [24-28] and formation of vanadium-deficient layers [29] were also reported as other strategies to enhance the

photocatalytic CO_2 reduction on $BiVO_4$. Despite the well-known importance of engineering the defects and lattice strain on photocatalytic CO_2 conversion, there have been limited studies on this issue for pure $BiVO_4$ without the addition of impurities.

There are some reported methods in the literature to introduce the defects and strain in photocatalysts. Thermal treatment under hydrogen or inert atmospheres at high temperature, chemical reduction, vacuum activation, ultraviolet irradiation, phase transformation via fast heating, plasma etching, lithium-induced conversion and low-valence metal doping are some methods used to introduce lattice defects such as oxygen vacancies [30-32]. Most of these methods need chemical reactions, high temperature or impurity addition. In the case of $BiVO_4$ for photocatalytic CO_2 conversion, doping with other elements or producing oxygen- and vanadium-deficient layers by chemical reactions are the methods utilized for oxygen vacancy generation [24-29]. There are few studies on strain engineering of $BiVO_4$-based photocatalysts, although strain engineering can be conducted by the formation of layered and core-shell structures or by chemical methods such as solvothermal technique [11,12].

In this study, $BiVO_4$ was treated by a high-pressure torsion (HPT) method to simultaneously introduce both defects and strain and improve the electronic structure, carrier dynamics and photocatalysis CO_2 conversion. The HPT method, in which a material is torsionally strained under high pressure [33], was used in this study because the method can introduce defects and strain in oxides without a need for impurity atoms [34,35]. The highly-strained and oxygen-deficient $BiVO_4$ exhibited narrow optical bandgap, enhanced conduction band bottom, low electron-hole recombination rate and high photocatalytic CO_2 conversion, which was comparable to the conversion rate on P25 TiO_2 as a benchmark photocatalyst. This study introduces an effective strategy based on defect and strain engineering to enhance the photocatalytic CO_2 conversion on $BiVO_4$, although the strategy is easily applicable to a wider range of photocatalysts for CO_2 conversion.

2. Experimental procedure

2.1. Sample synthesis

Initial $BiVO_4$ with 99.9% purity was purchased from Sigma Aldrich and further processed by HPT, as schematically shown in Fig. 1a [33]. For HPT processing, about 410 mg of initial powder was first compressed under 380 MPa to form pellets with 10 mm diameter and 0.8 mm thickness. The pellets were then compressed between two HPT anvils under a pressure of 6 GPa at room temperature (300 K). When the pressure was stabilized, the sample was plastically strained by rotating the lower anvil with respect to the upper anvil for either 0.25, 1 or 4 turns with a rotation speed of 1 rpm. It should be noted that larger plastic deformation is introduced in the sample with increasing the number of HPT turns [33]. The appearance of the initial powder and of the three samples processed by HPT after compacting to disc shapes are shown in Fig. 1b. The color of samples became darker with increasing the number of HPT turns and changed from yellow to orange and rose, respectively. These color changes indicate that photons with lower energies can be absorbed after HPT processing, as shown in the Itten color wheel of Fig. 1c [36].

2.2. Characterization

The initial powder and the samples processed by HPT for 0.25, 1 and 4 turns were characterized by various techniques, as described below.

- Crystal structure was examined by X-ray diffraction (XRD) utilizing the Cu Kα radiation (λ = 0.1542 nm wavelength) and a zero-diffraction amorphous silicon holder with a scanning speed

of 1 °/min. A Rigaku SmartLab 9kW AMK machine equipped with automatic alignment systems for beam, detector and sample (height and angle) was used for the XRD analysis. The precision of diffraction angle, confirmed by using a standard crystalline silicon sample, was better than 0.01°. XRD profiles were analyzed using PDXL software to determine the lattice parameters and lattice volume. Moreover, the crystallite size was determined by the Halder-Wagner method [37].

$$\left(\frac{\beta}{\tan^2\theta}\right)^2 = \frac{K\lambda}{D}\left(\frac{\beta\cos(\theta)}{\sin^2\theta}\right) + 16\varepsilon^2 \quad (1)$$

where, β, θ, K, λ, D and ε are full width at half maximum after subtracting the instrumental broadening, Bragg angle, shape factor, wavelength, crystallite size and lattice distortion (caused by planar and line defects), respectively.

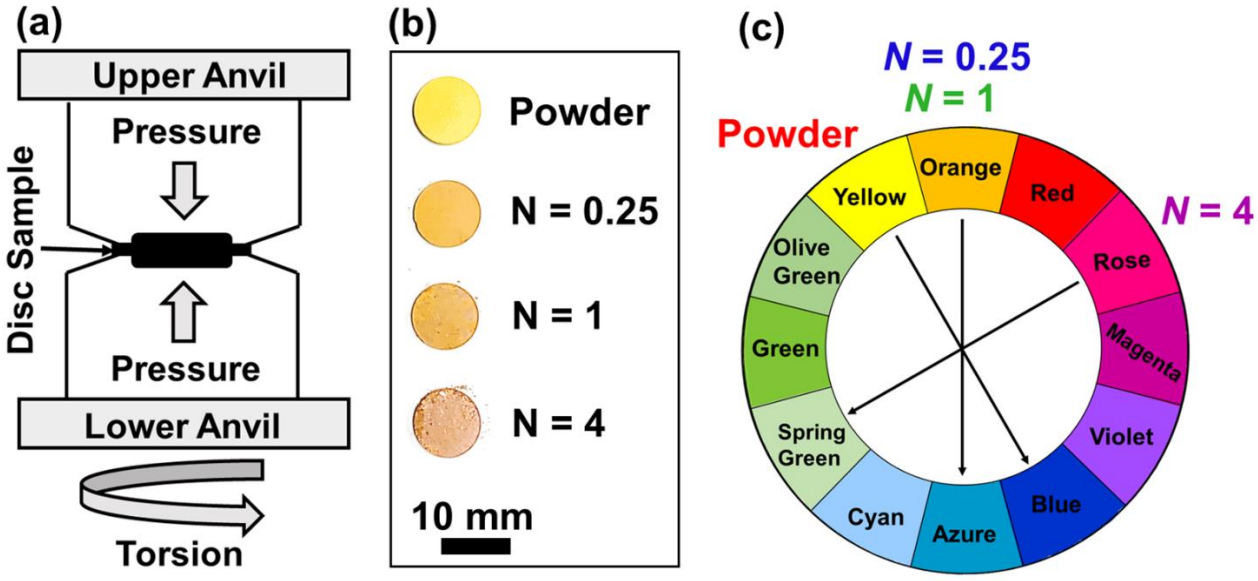

Fig. 1. (a) Schematics of HPT method, (b) appearance of $BiVO_4$ samples before and after HPT processing for 0.25, 1 and 4 turns, and (c) color of samples in comparison with Itten color wheel. Samples in (b) were compacted to disc form to show color changes clearly.

- Crystal structure was also examined by Raman spectroscopy using a laser source with λ = 532 nm wavelength. A Renishaw inVia Raman WiRE 4 machine equipped with an optic alignment tool was used. The precision of Raman shift, confirmed using a standard single-crystal silicon sample, was better than 0.1 cm^{-1}.
- Particle size was measured by the dynamic light scattering (DLS) method utilizing a Zetasizer Nano-S machine equipped with a 4 mW He-Ne laser (633 nm) with 173° diffraction angle. The specific surface area was measured from the average particle size as: surface area (m^2g^{-1}) = 6000 / [average particle size (nm) * (density (gcm^{-3})].
- Microstructure was investigated by transmission electron microscopy (TEM) using the bright-field (BF) images, dark-field (DF) images, selected area electron diffraction (SAED) analysis, high-resolution images and fast Fourier transform (FFT) diffractograms. For these observations, small amounts of samples were crushed in ethanol and dispersed on a carbon grid and examined in an aberration-corrected TEM under a voltage of 200 keV.

- X-ray photoelectron spectroscopy (XPS) using the Al Kα radiation with a wavelength of λ = 0.834 nm was used to determine the oxidation state of elements and the presence of oxygen vacancies. Peak deconvolution of O 1s XPS spectrum was also performed to calculate the oxygen vacancies concentration [38].
- Electron paramagnetic resonance (EPR) using a 9.4688 GHz microwave source was used to investigate the formation of oxygen vacancies.
- Light absorbance of samples was examined by UV-vis diffuse reflectance spectroscopy and then the optical bandgap was calculated by the Kubelka-Munk analysis.
- The valence band top was determined using the ultraviolet photoelectron spectroscopy (UPS) with the He-I UV irradiation and a DC bias of -4 V. The conduction band bottom was determined by adding the bandgap to the valence band top.
- Recombination rate of electrons and holes was investigated by steady-state photoluminescence (PL) emission spectroscopy with a 325 nm laser light source.
- Time-resolved photoluminescence decay (PL decay) with a 285 nm laser source was performed to investigate the average lifetime of excited electrons.

2.3. Photocurrent test

Photocurrent measurement was conducted under the full arc of a xenon lamp (300 W, Asashi Spectra, Japan, HAL-320W) in a 1 M Na_2SO_4 electrolyte to study the electron separation potential. A thin film of $BiVO_4$ samples on FTO (fluorine-doped tin oxide, 8 Ω/sq, Aldrich) glass was used as a working electrode, and Pt wire and Ag/AgCl were utilized as the counter and reference electrodes, respectively. To measure the photocurrent generation, an electrochemical analyzer (ALS C. Ltd., Japan, BAS1230C) was used in potentiostatic amperometry mode under a voltage of 0.7 V versus Ag/AgCl (0.5 min light ON and 1 min light OFF). To prepare the thin film samples, 5 mg of $BiVO_4$ were crushed in 0.2 mL ethanol and dispersed on 2.25 mm thick FTO glass with 15×25 mm^2 surface area and baked in a muffle furnace at 473 K for 1 h, as described in detail in an earlier study [39].

2.4. Photocatalysis test

For the photocatalytic CO_2 conversion test, 120 mg of each sample was dissolved in 500 mL of deionized water and 1 M $NaHCO_3$ under CO_2 bubbling with a flow rate of 3 $mLmin^{-1}$. Photocatalytic test was performed in an 858 mL cylindrical quartz photoreactor with continuous flow, as described earlier [40]. A high-pressure mercury light source with 0.5 Wcm^{-2} light intensity (Sen Lights continuous flow Corporation, HL400BH-8, 400 W) with no filtering was used for irradiation. The process was first performed without irradiation for 2 h to be sure about the absence of reaction products. The light source was then placed in the inner space of the reactor and the reactor temperature was adjusted to 288 K by a water chiller. The reaction mixture was stirred continuously by a magnetic stirrer and the CO_2 gas was injected into the reactor by an inlet hole on the top of the reactor. The reaction products continuously flowed out of the reactor through an outlet hole on the top of the reactor, as shown in Fig. 1a. The outlet gas from the reactor was divided into two parts and moved either to vent or a gas chromatograph (Shimadzu GC-8A, Ar Carrier). The formation of CO and CH_4 was determined by a flame ionization detector equipped with a methanizer (Shimadzu MTN-1). To measure H_2 and O_2 production rate, a thermal conductivity detector was also used. Fig. 2a shows the system used for photocatalytic CO_2 conversion along with the relevant spectral composition of the mercury light source in Fig. 2b. It

should be noted that a blank test without the catalyst addition but with light irradiation was also conducted to be sure about the absence of reaction products.

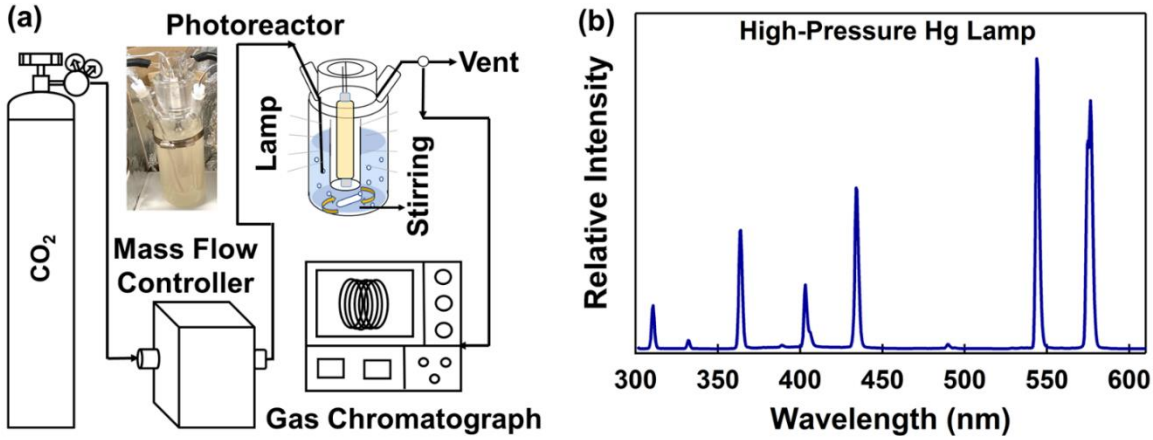

Fig. 2. (a) Schematics of photocatalytic experiment for CO_2 conversion, (b) spectral composition of light source employed for photocatalytic experiment.

3. Results

3.1. Lattice strain and microstructure

Fig. 3a shows the crystal structure analysis of four samples using the XRD method. It is evident that the initial powder and the HPT-processed samples have a monoclinic phase (C12/c1 space group with a = 0.519 nm, b = 1.170 nm, c = 0.509 nm; α = 90°, β = 90.38° and γ = 90°). XRD profiles in a higher magnification are shown in Fig. 3b for the (004) atomic plane with a diffraction angle of ~30.5°. There is a peak shift to higher angles after HPT processing and the shift becomes more significant with increasing the number of turns (i.e., with increasing plastic deformation). The peak shift is an indication of lattice expansion, which can be due to lattice strain and vacancy-type defect formation [41,42]. Furthermore, a peak broadening occurs, and the broadening becomes more significant with increasing the number of turns. The peak broadening is usually due to the formation of dislocation-type defects or planar imperfections such as grain boundaries [43]. Fig. 3c shows the crystallite size of four samples measured by the Halder-Wagner method. It is evident that the crystallite size increases from 65.7 nm for the initial powder to 24.6, 12.2 and 8.8 nm for the samples proceeded by HPT for 0.25, 1 and 4 turns, respectively. Fig. 3a also summarizes the volumetric lattice strain which was calculated as the increase in the lattice volume of the HPT-processed sample compared to the lattice volume of the initial powder, $\Delta V/V_0$. The estimated volumetric lattice strains for the samples proceeded by HPT for 0.25, 1 and 4 turns are 0.52%, 0.68% and 0.86%, respectively.

Fig. 4a illustrates the crystal structure analysis using the Raman spectroscopy method for the four samples. All peaks in the Raman spectra correspond to the monoclinic phase in good agreement with the XRD analyses. The peaks located at 124 and 210 cm^{-1} are relevant to the external mode of $BiVO_4$; the peaks located at 330 and 365 cm^{-1} are relevant to asymmetric (($\delta_{as}(VO_4^{-3})$) and symmetric (($\delta_s(VO_4^{-3})$) deformation modes of the VO_4^{3-}, respectively; and the peak located at 827 cm^{-1} is due to stretching vibration mode of the V-O bonds in the VO_4^{-3} (υ_s) [44]. Since the peak at 827 cm^{-1} shows the length of V-O bonds, it is usually used to analyze the lattice strain in $BiVO_4$ [45]. Fig. 4b shows the Raman spectra of stretching vibration mode of the V-O bonds in higher magnification. It is evident that there is a peak shift to the lower wavenumbers

after HPT processing and the shift is enhanced by increasing the number of turns. This shift indicates that a lattice expansion (tensile strain) occurs in the samples [46].

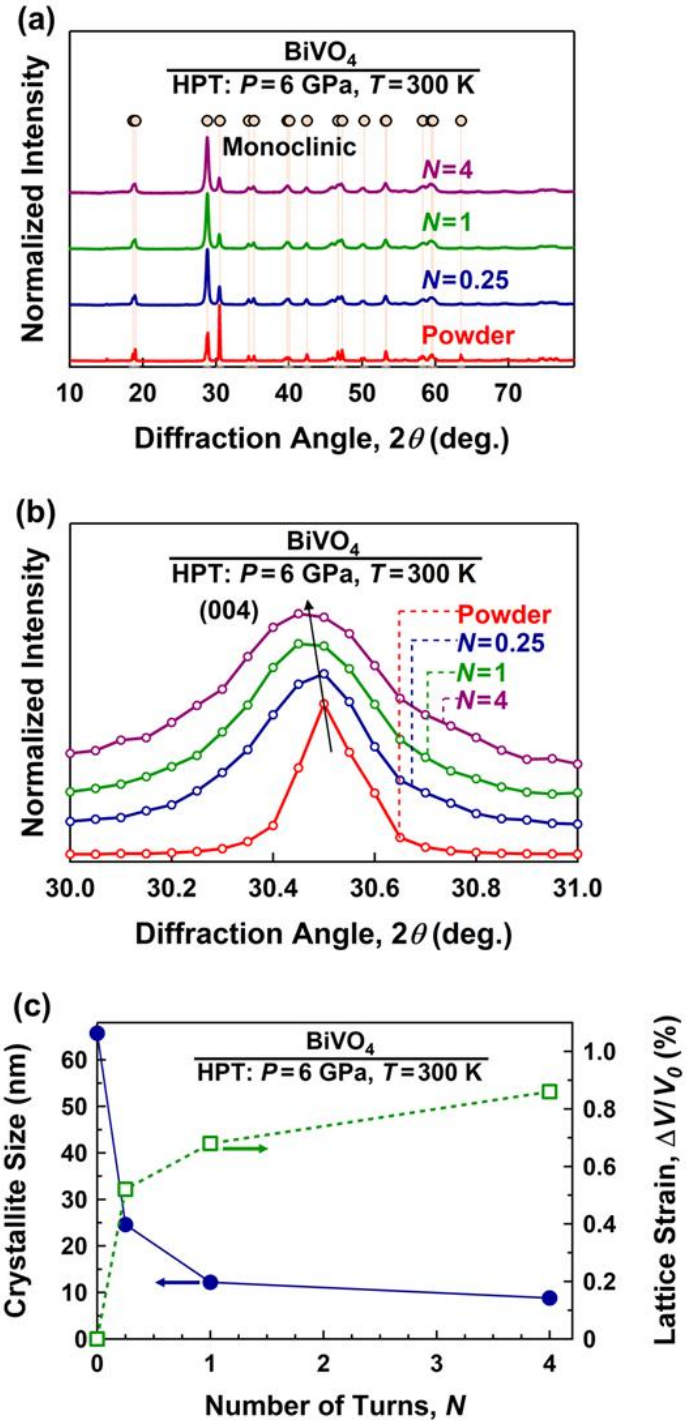

Fig. 3. Formation of strained nanocrystals in monoclinic phase $BiVO_4$ by HPT processing. (a) XRD analysis, (b) XRD analysis in high magnification for (004) atomic plane and (c) crystallite size and volumetric lattice strain versus number of HPT turns for powder and samples processed for 0.25, 1 and 4 turns.

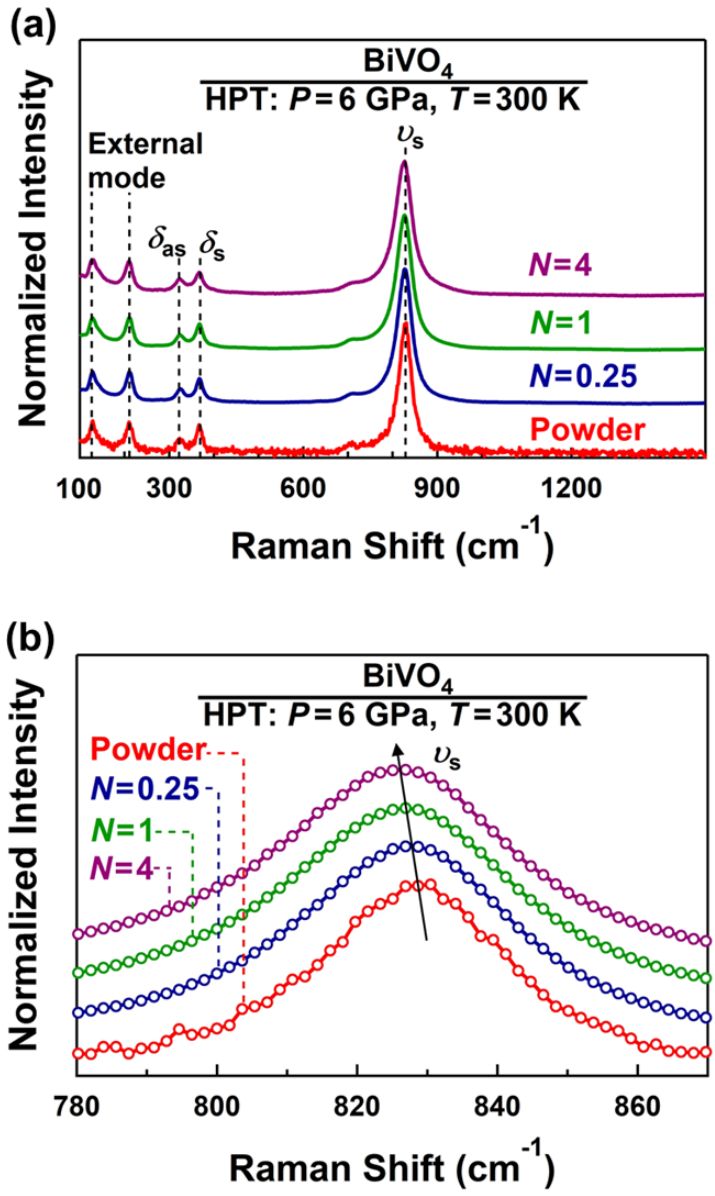

Fig. 4. Introduction of lattice strain in $BiVO_4$ by HPT processing. (a) Raman spectroscopy, and (b) Raman spectroscopy in high magnification for stretching vibration mode of V-O bonds for initial powder and samples processed for 0.25, 1 and 4 turns.

The distribution of particle size of the four samples measured by DLS is shown in Fig. 5. The average particles size for the initial powder is 370 nm, but it increases to 420, 540 and 540 nm after HPT processing for 0.25, 1 and 4 turns, respectively. It is concluded that despite decreasing the crystallite size by HPT processing, the specific surface area decreases after HPT processing: 3.8 m^2g^{-1} for the initial powder and 3.4, 2.6 and 2.6 m^2g^{-1} for the samples processed by HPT for 0.25, 1 and 4 turns, respectively. Such a decrease in specific surface area, which is a consequence of high applied pressure and large plastic deformation, was reported in a wide range of HPT-processed materials [33,34].

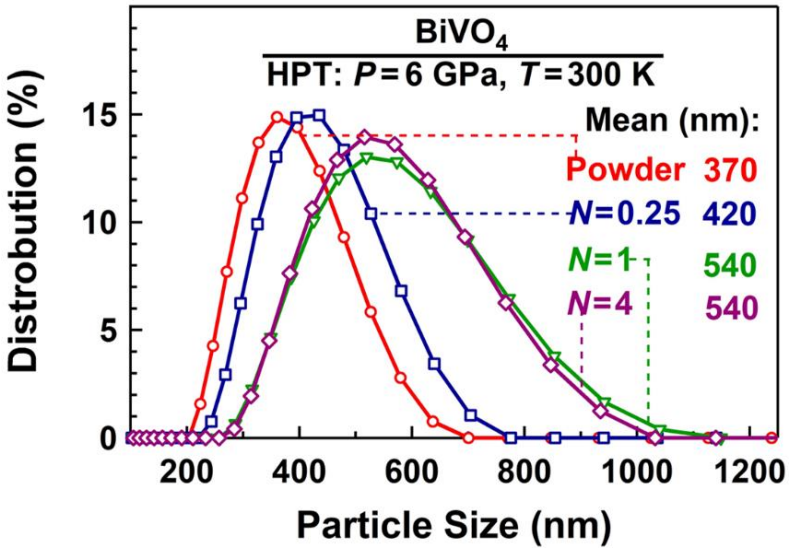

Fig. 5. Increasing average particle size of $BiVO_4$ by HPT processing. Particle size distribution, determined using DLS method, for initial powder and samples processed for 0.25, 1 and 4 turns.

Fig. 6 shows the microstructure analysis by TEM for four samples in the BF, DF and SAED modes. It should be noted the dark and bright colors in the BF and DF images are due to the diffraction contrasts. The white regions in the DF images correspond to grains having the diffracted beam indicated by arrows in the SAED profiles. The SAED profile has a dotted pattern, and only one grain with the submicrometer size is observed in the initial powder. After HPT processing for 0.25 turns, a combination of doted and ring patterns is observed in the SAED profiles, indicating grain refinement to the nanometer sizes partially occurs, as is also evident in the DF images with some nanosized white regions. The ring pattern of SAED analyses after 1 and 4 turns and the presence of many white nanosized regions in DF images confirm that the initial submicrometer grain sizes are refined to the nanometer sizes. The average grain size after 4 HPT turns is 15 nm, which is in reasonable agreement with the crystallite size value measured by the XRD analysis in Fig. 3c. Such a decrease in the crystal size is a consequence of large plastic deformation, as reported in a wide range of HPT-processed oxides [34,35,39].

The nanostructural evolution is shown more clearly in Fig. 7 using the TEM high-resolution images for (a) the initial powder, and for the samples processed by HPT for (b) 0.25, (c, d) 1 and (e, f) 4 turns. The high-resolution images confirm the presence of monoclinic lattice structure in all samples in good agreement with the XRD analysis and Raman spectroscopy. Moreover, while the initial powder contains large crystals, numerous nanograins are formed after HPT processing. In addition to the formation of nanograins with high-angle grain boundaries, dislocations are also detected within some crystals, as shown in Fig. 7d. The presence of large fractions of grain boundaries and dislocations and resultant lattice distortion is consistent with the XRD peak broadening. The evolution of nanostructure to a defective and distorted state is supposed to contribute to an easier electron and hole separation in this material [31].

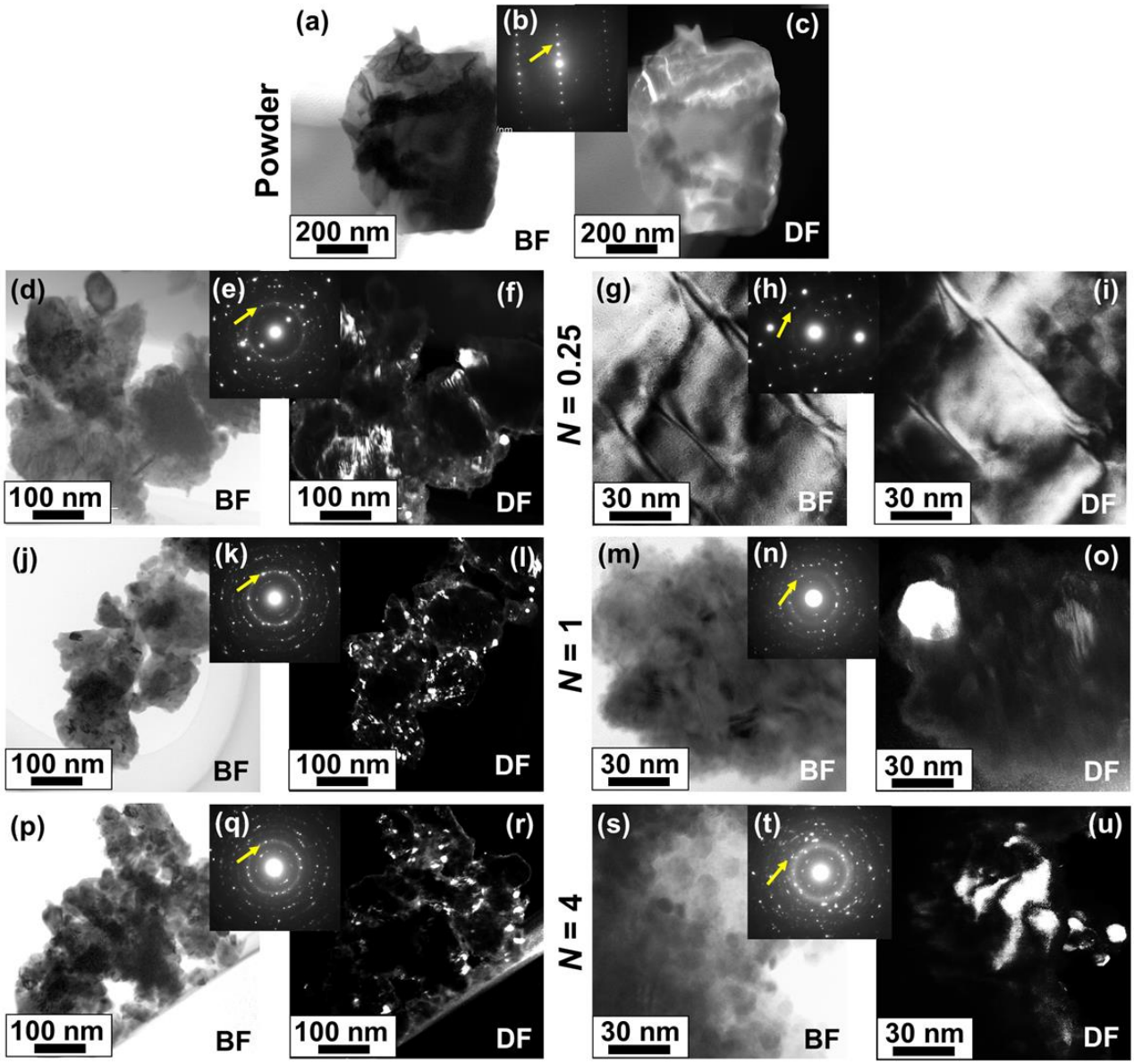

Fig. 6. Formation of nanograins in $BiVO_4$ by HPT processing. TEM BF images, SAED analyses and DF images taken with diffracted beams indicated by arrows in SAED analyses for (a-c) initial powder and samples processed for (d-i) 0.25, (j-o) 1 and (p-u) 4 turns.

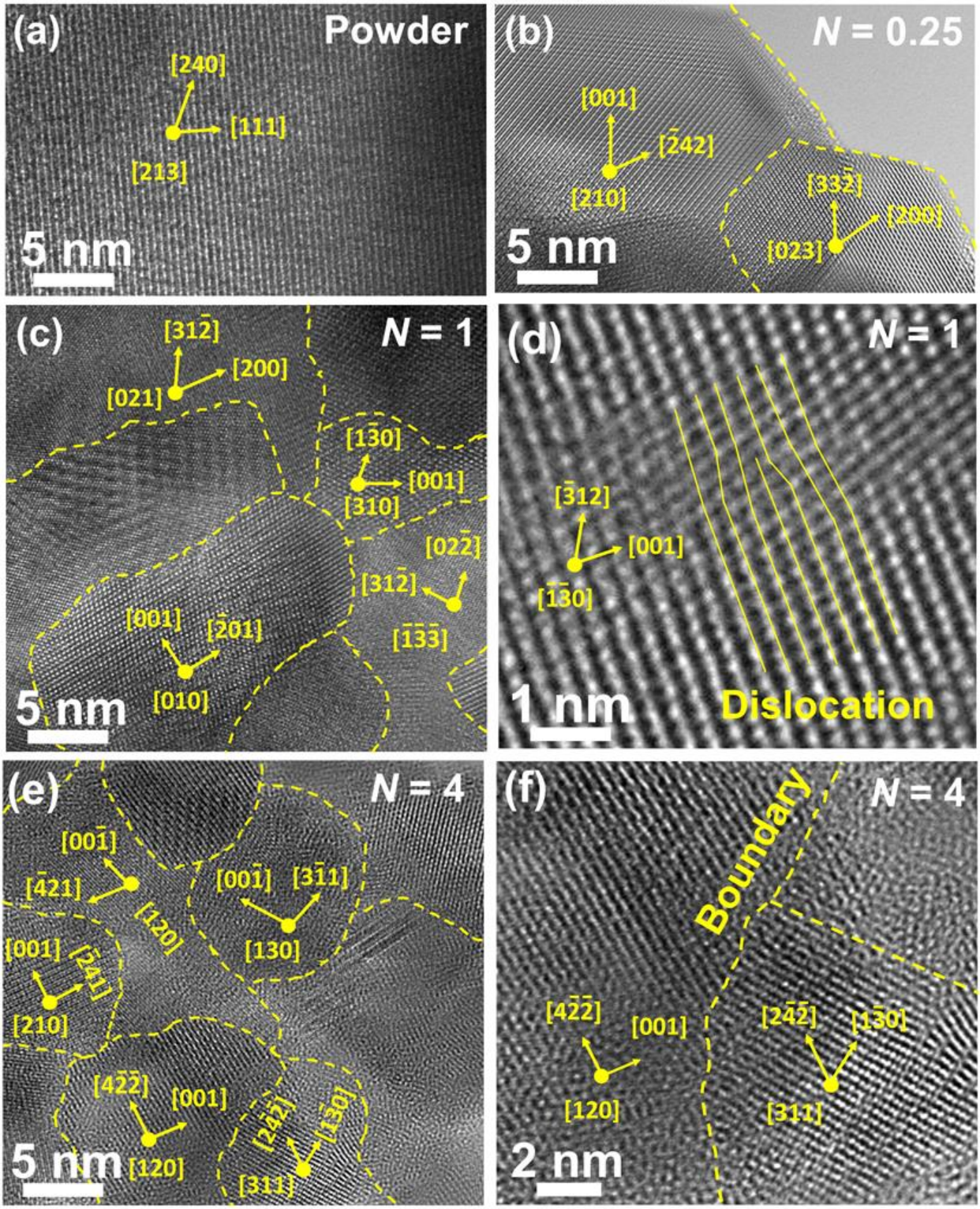

Fig. 7. Coexistence of grain boundaries and dislocations in $BiVO_4$ after HPT processing. TEM high-resolution images for (a) initial powder and for samples processed for (b) 0.25, (c, d) 1 and (e, f) 4 turns.

3.2. Oxygen vacancy formation

The changes of the color of samples from yellow for the initial powder to orange for the samples processed with 0.25 and 1 turns and to rose for the sample processed with 4 turns (Fig. 1c) indicates that the color centers such as oxygen vacancies should have formed after HPT processing [39]. The lattice expansion, confirmed by XRD peak shift in Fig. 3b and by Raman spectroscopy in Fig. 4b, also indirectly suggests that vacancy-type defects can be formed by HPT processing [41,42,45]. In addition to these evidences, the presence of oxygen vacancies can be analyzed by XPS and EPR analyses.

The XPS spectra of initial powder and samples processed by HPT are shown in Fig. 8 for (a) Bi 4f, (b) V 2p and (c) O 1s. Examination of XPS data confirms that the main oxidation states of three elements are Bi^{3+}, V^{5+} and O^{2-}. The Bi 4f and V 2p spectra do not show a clear change after HPT processing. However, the O 1s spectra in Fig. 8c after HPT processing show small shoulders at high energies, indicating the formation of oxygen vacancies [38]. To quantify, the concentration of oxygen vacancies using XPS, peak deconvolution for the O 1s spectra was conducted by considering two components in the spectra: (i) oxygen at lattice sites O_L, and (ii) oxygen vacancies O_V. The peak positions for O_L and O_V in Fig. 8c were considered at 529.9 and 530.7 eV, respectively [47,48]. It is evident that the intensity of oxygen vacancy peak systematically increases with increasing the number of HPT turns. The intensity ratio for O_V to O_V+O_L, as an indication for surface oxygen vacancy concentration, is plotted in Fig. 8d for the four samples. The concentration of surface oxygen vacancy reaches ~15% after HPT processing for 4 turns, although this value may be overestimated due to the influence of adsorbed oxygen on O 1s spectra [49].

The EPR spectra for the four samples are shown in Fig. 8e, in which the electron spin resonance intensity is plotted against the dimensionless magnetic moment or g factor ($g = h\nu/\mu_B B_0$, h: Planck constant, ν: frequency, μ_B: magnetic field; B_0: Bohr magneton constant [50,51]). For all samples, peak pairs with opposite curvatures are observed, while the intensity of these peaks increases with increasing the number of HPT turns. For the sample processed for 4 turns, the turning points of these peaks are close to a g factor of 2. Since it was reported that a g factor of 1.978 for $BiVO_4$ corresponds to oxygen vacancies [52], it is concluded that some amounts of oxygen vacancies are present after HPT processing and particularly after 4 turns. The formation of vacancies by HPT processing, which was reported in both metallic [53,54] and non-metallic materials [35,36], is due to the plastic deformation effects on vacancy formation and due to the high-pressure effects on suppressing the vacancy annihilation.

3.3. Electronic structure

UV-vis spectroscopy and UPS analysis were employed to examine the light absorbance, bandgap and electronic band structure of $BiVO_4$. Fig. 9a shows the light absorbance of the four samples. All samples mainly absorb the light in the UV region, but the light absorbance in the visible region improves after HPT processing and particularly after 4 turns, indicating a better electron-hole separation after HPT processing. Light absorbance edge tends to transfer from the blue light region to the green light region after HPT processing for 4 turns, which is in agreement with the prediction of the Itten color wheel in Fig. 1c. The Kubelka-Munk analysis is shown in Fig. 9b for estimation of the direct bandgap. A bandgap narrowing occurs by HPT processing and the bandgap decreases from 2.4 eV for the initial powder to 2.3 eV for the samples processed with 0.25 and 1 turns and to 2.1 eV for the sample processed with 4 turns. Since no phase transformations occur in $BiVO_4$ by HPT processing, such a bandgap narrowing should be due to the introduction of lattice defects and strain [7-11].

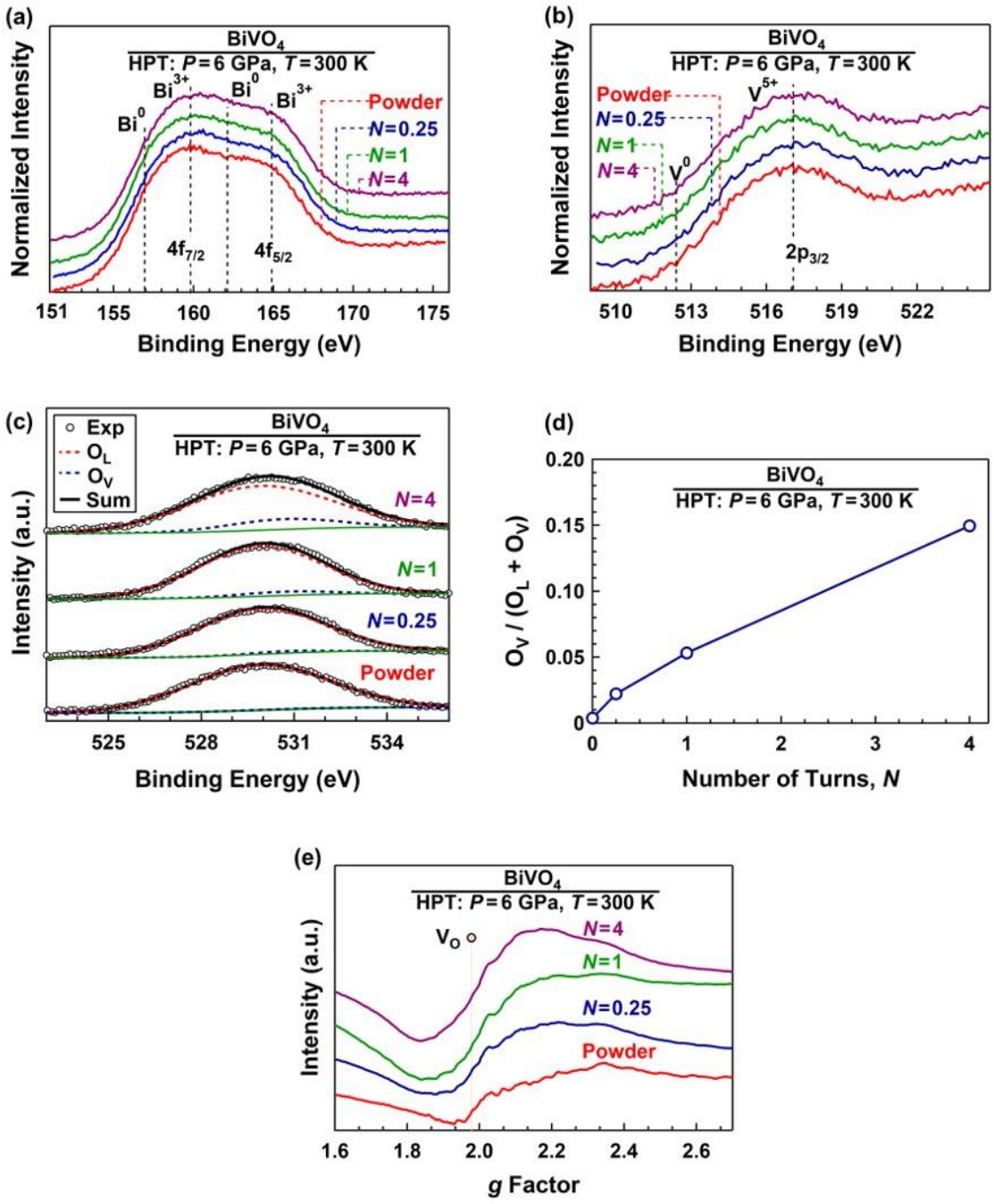

Fig. 8. Formation of oxygen vacancies in $BiVO_4$ after HPT processing. XPS spectroscopy of (a) Bi 4f, (b) V 2p and (c) O 1s and its peak deconvolution; (d) ratio of surface oxygen vacancy peak (O_V) to sum of lattice oxygen and vacancy peaks (O_L + O_V) plotted versus number of HPT turns; and (e) EPR spectroscopy for initial powder and samples processed for 0.25, 1 and 4 turns.

Fig. 9c shows the UPS spectra of four samples which are used to determine the top of the valence band from the vacuum level. The top of the valence band from the vacuum level was calculated as cutoff energy from the Fermi level (E_0 indicated by arrows in Fig 9c) - valence band top energy from the Fermi level (E_B indicated by arrows in Fig. 9c) - UV He-I energy (21.2 eV)

[55]. The top of the valence band for the initial powder and the samples processed by HPT for 0.25, 1 and 4 turns is -6.4, -6.0, -6.0 and -6.0 eV versus the vacuum level, respectively. By the addition of bandgap values to the top of the valence band, the bottom of the conduction band can be determined as -4.7, -3.7, -3.7 and -3.9 eV for the initial powder and the samples processed by HPT for 0.25, 1 and 4, respectively. Fig. 9d shows the band structure of four samples, while the numbers in the figure are the positions of the top of the valence band and the bottom of the conduction band versus the normal hydrogen electrode (NHE): energy vs. NHE = -4.4 - energy vs. vacuum [55]. For the initial powder, the bandgap, the top of the valence band and the bottom of the conduction band are in agreement with the reported data in the literature [56]. After HPT processing, in addition to bandgap narrowing the bottom of the conduction band increases, suggesting that the problem of low conduction band bottom of $BiVO_4$ [17,18] can be successfully solved by the introduction of lattice defects and strain. As shown in Fig. 9d, the electronic structure of all four samples can support the CO_2 conversion reactions by considering the relevant chemical potentials for different reactions [4,5]. However, the HPT-processed samples have a higher overpotential for CO_2 conversion, which is thermodynamically desirable for photocatalysis. While earlier studies used the heterojunctions to solve the problem of the electronic structure of $BiVO_4$ [18-23], this study confirms that engineering the lattice defects and strain is effective to improve the electronic structure of pure $BiVO_4$ without any need for a second phase or impurity atoms.

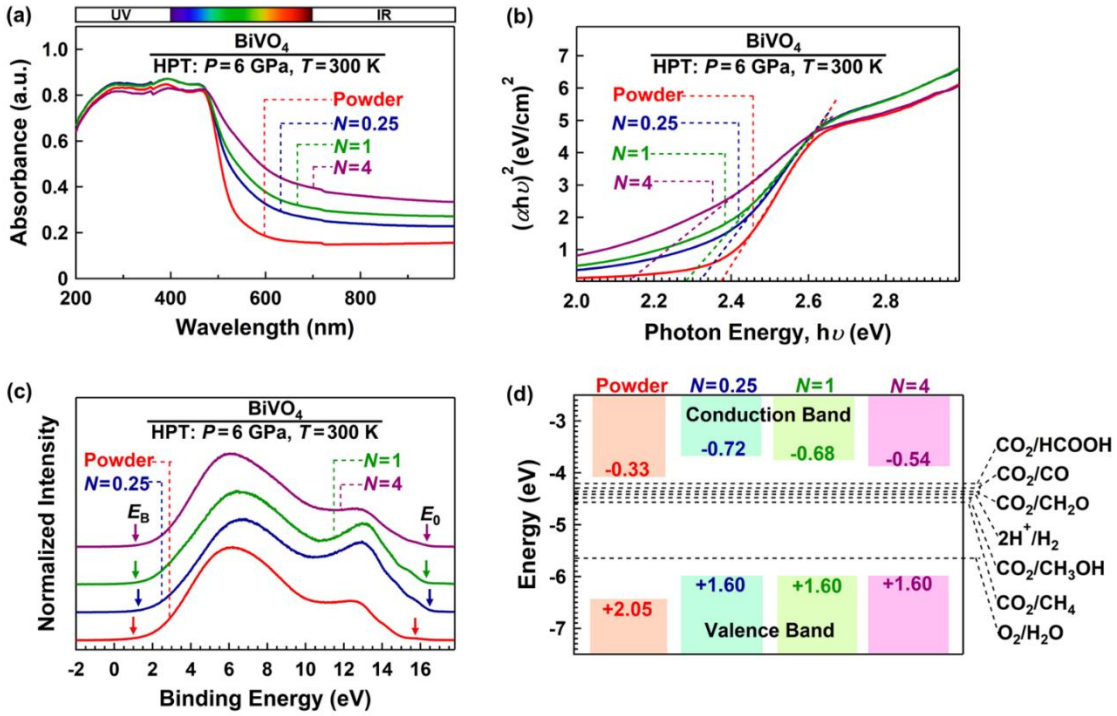

Fig. 9. Bandgap narrowing and improvement of electronic band structure of $BiVO_4$ for photocatalytic CO_2 conversion by HPT processing (a) UV-vis spectroscopy, (b) Kubelka-Munk analysis for direct bandgap calculation (α: light absorption, h: Planck's constant, ν: photon frequency), (c) UPS spectroscopy using bias of -4 V to measure the top of the valence band, and (d) electronic band structure including chemical potentials for CO_2 reduction reactions for initial powder and samples processed for 0.25, 1 and 4 turns. Arrows on left and right in (c) indicate the valence band top energy (E_B) and cutoff energy (E_0) shifted 4 eV lower from Fermi level, respectively. Numbers in (d) shows energy levels versus normal hydrogen electrode (NHE).

3.4. Charge carrier dynamics

Fig. 10 shows (a) PL spectroscopy, (b) PL decay analysis and (c) photocurrent measurements which can give information about charge carrier dynamics including the recombination of electrons and holes, mobility of charge carriers and defect trapping [5]. Fig. 10a shows a significant decrease in PL intensity after HPT processing, indicating that the recombination rate of electrons and holes decreases effectively after HPT processing. These results suggest that the HPT-induced defects and strain act positively as electron-hole separation sites rather than recombination sites [19,26,39]. The PL peak for all samples appeared at a peak around 650 nm (1.9 eV) which is less than the bandgap of samples. Although electron-hole recombination in $BiVO_4$ can happen radiatively or nonradiatively, the emission detected around 650 nm in Fig. 10a was attributed to the radiative recombination of electrons and holes on defects [52,57].

PL decay spectra shown in Fig. 10b follow a relation shown below [58].

$$I(t) = A_1 \exp\left(-\frac{t}{\tau_1}\right) + A_2 \exp\left(-\frac{t}{\tau_2}\right) \quad (4)$$

where, $I(t)$, A_1, A_2, τ_1 and τ_2 are PL decay intensity at time t, the amplitude of the first exponential function, amplitude of the second exponential function, fast decay time and slow decay time, respectively. The average lifetime can be calculated using the following equation [58].

$$\tau_{ave} = \frac{A_1\tau_1^2 + A_2\tau_2^2}{A_1\tau_1 + A_2\tau_2} \quad (5)$$

Values of A_1, A_2, τ_1, τ_2 τ_{ave} for the initial powder and the samples processed by HPT are presented in Table 2. The average electron lifetime decreases from 12.90 ns for the initial powder to 11.48, 10.22 and 9.24 ns for the samples processed for 0.25, 1 and 4 turns, respectively. The decrease in the lifetime for HPT samples can be attributed to the formation of oxygen vacancies. Oxygen vacancies on the surface of photocatalyst act as shallow traps or active sites for the fast migration of electrons and participation in a reaction. Therefore, their formation can lead to a decrease in the exited electron lifetime and an increase in the photocatalytic activity [39,48]. It should be noted that the oxygen vacancies in the bulk can also lead to electron migration and a decrease in the lifetime, but they do not necessarily improve the photocatalytic activity [31,59,60].

Photocurrent measurements in Fig. 10c demonstrate that the current density is the highest for the initial powder and decreases with HPT processing and increasing the number of turns. Since photocurrent generation is attributed to the migration of electrons from the surface under an external voltage, Fig. 10c suggests that electron separation from the surface of $BiVO_4$ becomes weaker after HPT processing. Such a decrease in photocurrent may not be due to enhanced electron-hole recombination because the PL intensity (as an indication of recombination) decreases after HPT processing, as shown in Fig. 10a. The decreases in photocurrent density after HPT processing should be due to the action of surface vacancies as electron trapping sites. It was shown earlier that polarity and localization of photoexcited electrons of $BiVO_4$ can lead to electron trapping in this material [61]. Such trapping can be enhanced on oxygen vacancies, making these defects active sites with sufficient electrons for chemical reactions (particularly if they form near the bottom of the conduction band and act as shallow donors) [62]. Theoretical studies suggested that a change of the oxygen vacancy states from the shallow donors to localized intragap states can reduce the photoconductivity and photocurrent of $BiVO_4$ [62], but this is not the case in this study because the PL spectra in Fig. 10a show similar peak energies for all four samples.

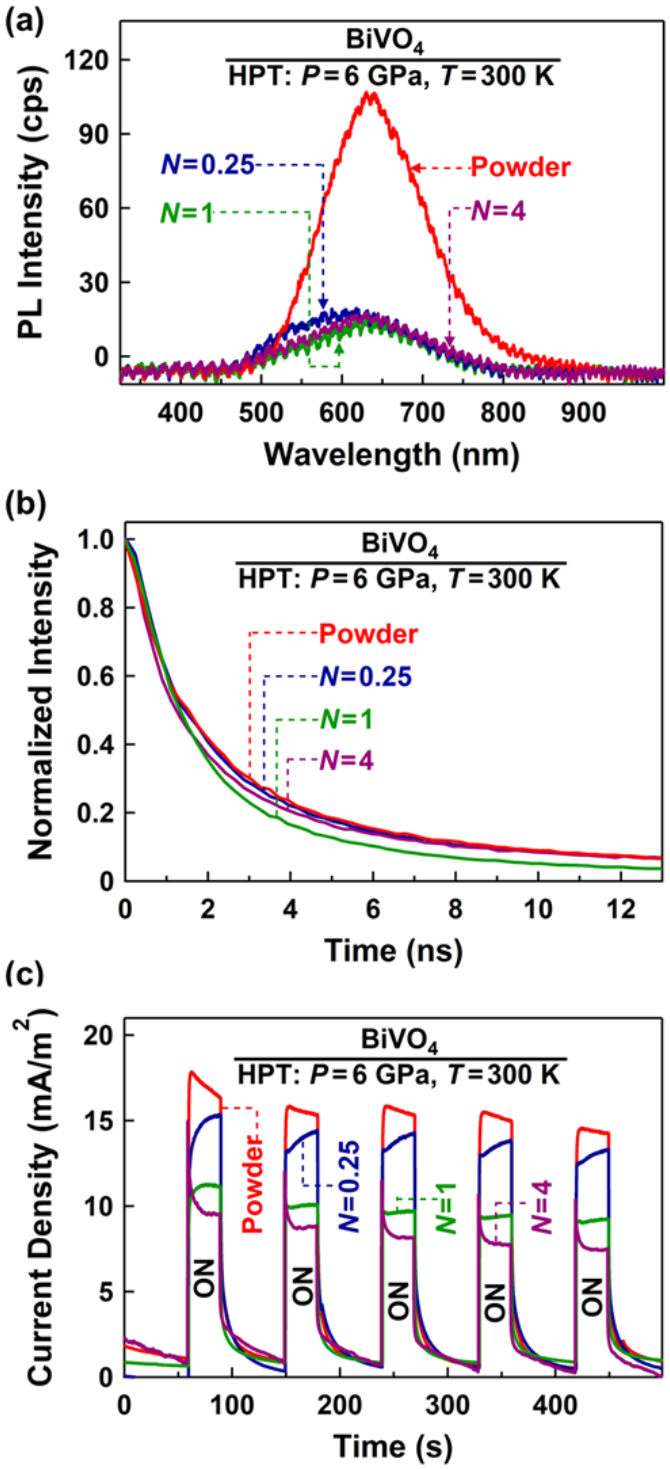

Fig. 10. Decreasing recombination of electrons and holes in $BiVO_4$ after HPT processing. (a) Steady-state PL emission spectra, (b) time-resolved PL decay spectra, and (c) photocurrent density versus time for initial powder and samples processed for 0.25, 1 and 4 turns.

Table 2. Decreasing electron lifetime in $BiVO_4$ by HPT processing. PL decay parameters and electron lifetimes for initial powder and for samples processed for 0.25, 1 and 4 turns.

Sample	τ_1 (ns)	τ_2 (ns)	A_1	A_2	τ_{ave} (ns)
Powder	2.17	14.92	56.56	43.44	12.90
N = 0.25	1.92	13.08	53.19	46.81	11.48
N = 1	1.78	12.40	64.26	35.74	10.22
N = 4	1.62	10.35	48.09	51.91	9.24

3.5. Photocatalytic activity

Photocatalytic CO_2 to CO conversion activity of the initial powder and the samples processed by HPT for 0.25, 1 and 4 turns are shown in Fig. 11a versus the catalyst mass unit and in Fig. 11b versus the catalyst surface area unit. Since the photocatalytic reactions occur on the surface of photocatalysts, normalizing the CO production rates per surface area is more reasonable to show the differences. It should be noted that the photocatalytic tests were conducted two times in Figs. 11a and 11b for the initial powder and for the sample processed with N = 4 to confirm the reproducibility of data. All samples could convert CO_2 to CO, but the photocatalytic performance of HPT-processed samples is better than the initial powder. The sample processed for 4 turns shows the highest activity. The average of CO production rate for the powder is 2.27 ± 0.24 $\mu molh^{-1}g^{-1}$ (0.60 ± 0.06 $\mu molh^{-1}m^{-2}$) which increases to 3.21 ± 0.23, 3.35 ± 0.27 and 3.97 ± 0.38 $\mu molh^{-1}g^{-1}$ (0.96 ± 0.07, 1.27± 0.10 and 1.45± 0.08 $\mu molh^{-1}m^{-2}$) for the samples proceeded for 0.25, 1 and 4 turns, respectively. Here, it should be noted that no hydrocarbons such as CH_4 and no oxidation products such as O_2 were detected within the detection limits of the experiments. The absence of the oxidation products should be a reason for the gradual decrease in the activity during the time. It should be mentioned that the result of the blank test before the photocatalytic activity test (addition of catalysts without light irradiation) shows that the production rate of CO is zero (the data point at t = 0 h). Moreover, a blank test without the addition of catalyst with light irradiation shows no CO production within 8 h, as shown in Fig. 11a and 11b. The improvement of photocatalytic activity of $BiVO_4$ after HPT processing should be due to the presence of oxygen vacancies as active sites for adsorption and conversion of CO_2 molecules as well as due to the effect of lattice strain on the improvement of band structure for CO_2 photoreduction [2,17].

Fig. 11c demonstrates the structure stability of powder and samples processed by HPT after photocatalytic test using the XRD analysis. All samples are stable and retain their monoclinic structure after use for photocatalytic CO_2 conversion. No chemical reaction, corrosion or degradation products are detected by XRD analysis. Since some photocatalysts are negatively influenced by photocorrosion phenomenon, finding the photocorrosion-resistant catalysts is a critical issue [63,64]. In some $BiVO_4$-based catalysts, it was reported that the photocorrosion and formation of bismuth oxides can occur by dissolving vanadium into the solution through the accumulation of holes on the surface [63,64]. The absence of such photocorrosion products confirms the stability of current HPT-processed photocatalysts.

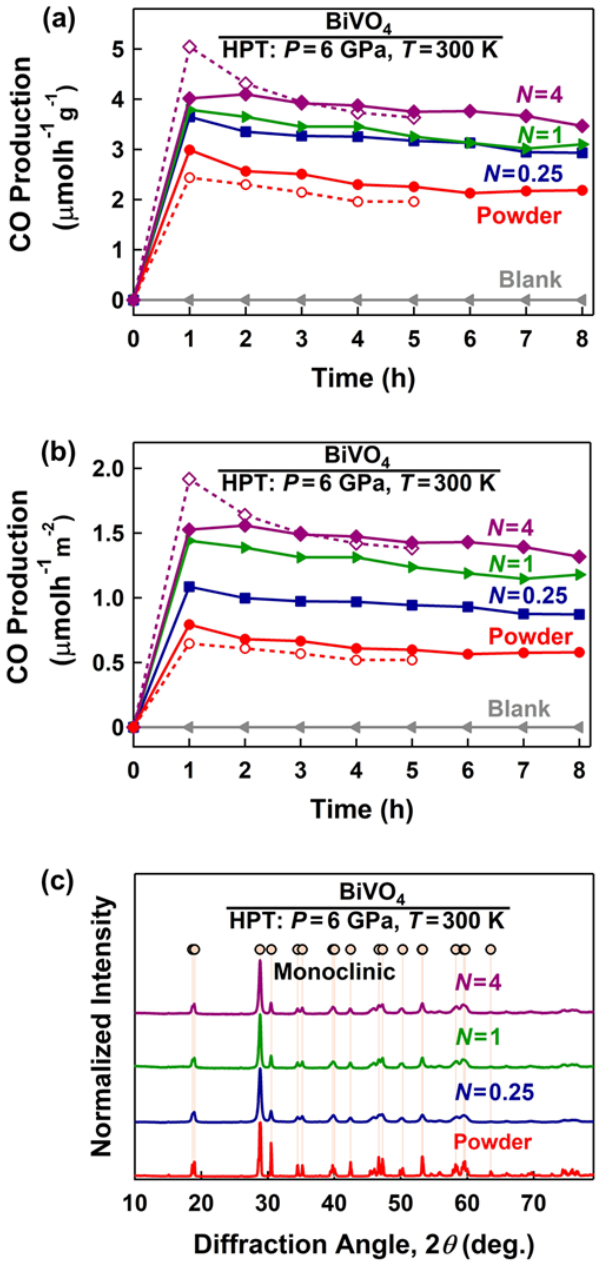

Fig. 11. Improvement of photocatalytic CO_2 conversion on highly-stable $BiVO_4$ after HPT processing. CO production rate under UV irradiation versus time normalized by (a) mass unit and (b) surface area of catalysts; and (c) XRD profiles after photocatalytic test for initial powder and samples processed for 0.25, 1 and 4 turns. Photocatalytic tests were repeated two times for initial powder and sample processed for 4 turns.

4. Discussion

This study shows that the simultaneous introduction of strain and oxygen vacancies into $BiVO_4$ can lead to improving the light absorbance, narrowing the bandgap, modifying the electronic band structure, decreasing the recombination rate of electrons and holes and finally enhancing the photocatalytic activity for CO_2 conversion. Unlike earlier strategies that mainly used heterojunctions [18-23] or doping [24-28] to deal with the low level of the conduction band in

$BiVO_4$ [17,18], this study shows that the level can be enhanced even in pure $BiVO_4$ by the accumulation of oxygen vacancies and lattice strain. Due to the presence of unpaired electrons in surface oxygen vacancies, they can act as adsorption sites to uptake CO_2 as a Lewis acid [8,65]. These vacancies also contribute to the activation of adsorbed CO_2 and H_2O for conversion to intermediate and final products by weakening the carbon-oxygen and oxygen-hydrogen bondings [8]. The oxygen vacancies on the surface do not usually act as recombination sites for electrons and holes, but they trap the excited electrons and provide active sites for photocatalytic reactions [65-67]. Here, it should be noted that the concentration of oxygen vacancies in $BiVO_4$ as activation sites should be an optimum level because large fractions of oxygen vacancies can reduce V^{5+} to V^{4+}, resulting in electron scattering due to a large ionic diameter of V^{4+} [42,68,69]. A high concentration of V^{4+} can lead to decreasing the length of effective diffusion of holes and accordingly reduce the photocatalytic activity [70]. Despite these expected effects of oxygen vacancies, the overall effect of oxygen vacancies in this study is the improvement of photocatalytic activity. On the other hand, lattice strain can lead to electronic band structure modification such as changing the level of the conduction band bottom or decreasing the bandgap [10-12]. Therefore, in the current HPT-processed $BiVO_4$ photocatalysts, increasing the light absorbance, decreasing the bandgap, and increasing the bottom of the conduction band energy are the results of the contribution of lattice strain, while decreasing the electron-hole recombination and improvement of surface catalytic activity are the main contribution of oxygen vacancies.

Here, to have a clear view regarding the improvement of photocatalytic CO_2 conversion of highly-strained and defective $BiVO_4$, some comparisons can be made. Fig. 12 compares the CO production rate of this material with P25 TiO_2, which is a typical benchmark photocatalyst. Note that both materials were examined exactly under similar conditions by the current authors. The average of photocatalytic CO production of P25 TiO_2 is 4.63 ± 0.33 $\mu molh^{-1}g^{-1}$ which is close to the productivity of HPT-processed $BiVO_4$ after 4 turns (3.97 ± 0.38 $\mu molh^{-1}g^{-1}$). Here, it should be noted that the surface area of P25 TiO_2 is 38.70 m^2g^{-1} which is much higher than the surface area of HPT-processed $BiVO_4$ (2.6 m^2g^{-1}). Despite the negative effect of the HPT method on the reduction of the surface area [34,41], Fig. 12 confirms the efficiency of the defect and strain engineering in improving the photocatalytic activity to high levels comparable with one of the most active photocatalysts. Another comparison is given in Table 3, in which photocatalytic activity of HPT-processed $BiVO_4$ was compared with some data for $BiVO_4$-based photocatalysts [19-28]. It should be noted that data in Table 3 should be compared with care because of the differences in experimental conditions in various studies (e.g., light source, photoreactor type, the mass of catalyst, etc.). Despite these differences, the range of reported photocatalytic CO production rate for these materials is between 0.05-13.5 $\mu molh^{-1}g^{-1}$, while the HPT-processed $BiVO_4$ shows one of the highest activities.

Finally, it is worth mentioning that the HPT method used in this study for the generation of defects and strain is applicable to any kind of conventional oxides [33,34] and multi-component ceramics and salts [71]. Although the method was used earlier by the authors to improve the photocatalytic CO_2 conversion by synthesis of high-pressure phases [40] or high-entropy oxides [41], its current application to introduce strain and defects is applicable to a wider range of materials to develop advanced photocatalysts for CO_2 conversion. Since the specific surface area is usually small after HPT processing, other alternative mechanical or chemical routes may be employed in the future for simultaneous generation of strain and defects in photocatalysts, while keeping their surface area large.

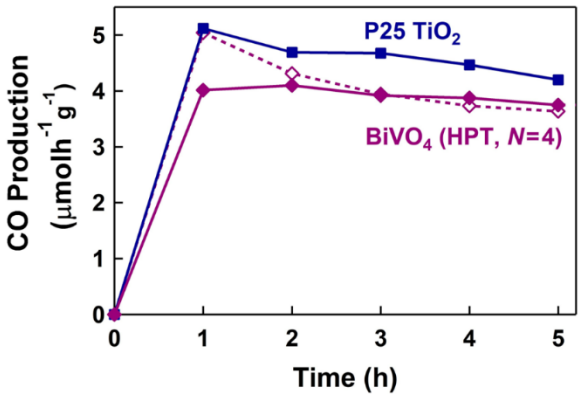

Fig. 12. High photocatalytic CO_2 conversion activity of highly-strained and oxygen-deficient $BiVO_4$ in comparison with P25 TiO_2 as benchmark photocatalyst. CO production rate versus irradiation time for $BiVO_4$ processed by HPT for 4 turns and P25 TiO_2.

Table 3. Photocatalytic CO evolution rate of $BiVO_4$ processed by HPT for 4 turns compared with other $BiVO_4$-based photocatalysts.

Photocatalyst	**Catalyst Mass (mg)**	**Light Source**	**CO Production ($\mu molh^{-1}g^{-1}$)**	**Reference**
$BiVO_4${110}-Au- Cu_2O	100	300 W Xe (> 420nm)	1.12	[19]
$BiVO_4${010}-Au- Cu_2O	100	300 W Xe (> 420nm)	2.02	[19]
$BiVO_4${010}-Cu_2O	100	300 W Xe (> 420nm)	0.45	[19]
$BiVO_4${010}-Au-(Cu_2O-Au)	100	300 W Xe (> 420nm)	2.08	[19]
$BiVO_4$-Cu_2O	------	300 W Xe (> 420nm)	~0.5	[20]
$BiVO_4$-C- Cu_2O	------	300 W Xe (> 420nm)	3.01	[20]
$ZnIn_2S_4$-$BiVO_4$	100	300 W Xe	4.75	[21]
$BiVO_4$-5 % $Bi_4Ti_3O_{12}$	10	300 W Xe	~6.75	[22]
$BiVO_4$-10 % $Bi_4Ti_3O_{12}$	10	300 W Xe	~13.5	[22]
$BiVO_4$-20 % $Bi_4Ti_3O_{12}$	10	300 W Xe	~6.75	[22]
Bi-$BiVO_4$	10	300 W Xe (> 420nm)	~0.75	[24]
Cu-Bi-$BiVO_4$	10	300 W Xe (> 420nm)	~11	[24]
$BiVO_4$	10	300 W Xe (> 420nm)	0.42	[26]
Bi-$BiVO_4$	10	300 W Xe (> 420nm)	1.29	[26]
Ag-Bi-$BiVO_4$ (Ag/Bi = 0.3)	10	300 W Xe (> 420nm)	3.4	[26]
Ag-Bi-$BiVO_4$ (Ag/Bi = 0.6)	10	300 W Xe (> 420nm)	5.19	[26]
Ag-Bi-$BiVO_4$ (Ag/Bi = 0.9)	10	300 W Xe (> 420nm)	4.54	[26]
1.0%Cu-$BiVO_4$	50	400 W High-Pressure Hg	2	[27]
0.5%Cu-$BiVO_4$	50	400 W High-Pressure Hg	4.1	[27]
0.3%Cu-$BiVO_4$	50	400 W High-Pressure Hg	3.9	[27]
Au-$BiVO_4$	50	300 W Xe (> 420nm)	~0.05	[23]
CdS-$BiVO_4$	50	300 W Xe (> 420nm)	~0.75	[23]
$Cd_{0.5}Zn_{0.5}S$-$BiVO_4$	50	300 W Xe (> 420nm)	~1.2	[23]
CdS-Au-$BiVO_4$	50	300 W Xe (> 420nm)	~1.1	[23]
$Cd_{0.2}Zn_{0.8}S$-Au-$BiVO_4$	50	300 W Xe (> 420nm)	~1.6	[23]
$Cd_{0.5}Zn_{0.5}S$-Au-$BiVO_4$	50	300 W Xe (> 420nm)	~2.15	[23]
$Cd_{0.8}Zn_{0.2}S$-Au-$BiVO_4$	50	300 W Xe (> 420nm)	~1.3	[23]
$BiVO_4$-2%Co	30	25 W 254 nm Ultraviolet	0.62	[28]
$BiVO_4$-5%Co	30	25 W 254 nm Ultraviolet	0.68	[28]
$BiVO_4$-10%Co	30	25 W 254 nm Ultraviolet	0.83	[28]
$BiVO_4$-15%Co	30	25 W 254 nm Ultraviolet	1.04	[28]
$BiVO_4$-20%Co	30	25 W 254 nm Ultraviolet	2.08	[28]
$BiVO_4$ (HPT: N = 4)	120	400 W High-Pressure Hg	3.97 ± 0.38	This study

4. Conclusion

A photocatalyst with low bandgap, improved band structure and low recombination rate of electrons and holes was produced by simultaneous introduction of oxygen vacancies and lattice strain in $BiVO_4$ via a high-pressure torsion process. The material showed high photocatalytic activity for CO_2 to CO conversion with an activity comparable to P25 TiO_2 as a benchmark photocatalyst. This study suggests that simultaneous engineering of lattice strain and defects is an effective strategy to produce active photocatalysts for CO_2 conversion.

Acknowledgments

This work is supported in part by the WPI-I2CNER, Japan, and in part by a Grants-in-Aid for Scientific Research on Innovative Areas from the MEXT, Japan (JP19H05176 & JP21H00150).

References

[1] W. Tu, Y. Zhou, Z. Zou, Photocatalytic conversion of CO_2 into renewable hydrocarbon fuels: state-of-the-art accomplishment, challenges, and prospects, Adv Mater 26 (2014) 4607–4626.

[2] K. Li, B. Peng, T. Peng, Recent advances in heterogeneous photocatalytic CO_2 conversion to solar fuels, ACS Catal. 6 (2016) 7485–7527.

[3] J. Ran, M. Jaroniec, S.Z. Qiao, Cocatalysts in semiconductor-based photocatalytic CO_2 reduction: achievements, challenges, and opportunities, Adv. Mater. 30 (2018) 1704649.

[4] X. Li, J. Yu, M. Jaroniec, Hierarchical photocatalysts, Chem. Soc. Rev. 45 (2016) 2603–2636.

[5] E. Kalamaras, M.M. Maroto-Valer, M. Shao, J. Xuan, H. Wang, Solar carbon fuel via photoelectrochemistry, Catal. Today 317 (2018) 56–75.

[6] S. Cao, B. Shen, T. Tong, J. Fu, J. Yu, 2D/2D heterojunction of ultrathin MXene/Bi_2WO_6 nanosheets for improved photocatalytic CO_2 reduction, Adv. Funct. Mater. 28 (2018) 1800136.

[7] J. Di, C. Zhu, M. Ji, M. Duan, R. Long, C. Yan, K. Gu, J. Xiong, Y. She, J. Xia, H. Li, Z. Liu, Defect-rich $Bi_{12}O_{17}C_{l2}$ nanotubes self-accelerating charge separation for boosting photocatalytic CO_2 reduction, Angew. Chem. 57 (2018) 14847–14851.

[8] K. Wang, J. Lu, Y. Lu, C.H. Lau, Y. Zheng, X. Fan, Unravelling the C-C coupling in CO_2 photocatalytic reduction with H_2O on Au/TiO_{2-x}: combination of plasmonic excitation and oxygen vacancy, Appl. Catal. B 292 (2021) 120147.

[9] M. Tahir, N. Aishah, S. Amin, Indium-doped TiO_2 nanoparticles for photocatalytic CO_2 reduction with H_2O vapors to CH_4, Appl. Catal. B 162 (2015) 98–109.

[10] Z. Liu, C. Menéndez, J. Shenoy, J.N. Hart, C.C. Sorrell, C. Cazorl, Strain engineering of oxide thin films for photocatalytic applications, Nano Energy 72 (2020) 104732.

[11] J. Di, P. Song, C. Zhu, C. Chen, J. Xiong, M. Duan, R. Long, W. Zhou, M. Xu, L. Kang, B. Lin, D. Liu, S. Chen, C. Liu, H. Li, Y. Zhao, S. Li, Q. Yan, L. Song, Z. Liu, Strain-engineering of $Bi_2O_{17}Br_2$ nanotubes for boosting photocatalytic CO_2 reduction, ACS Mater. Lett. 2 (2020) 1025–1032.

[12] X. Cai, F. Wang, R. Wang, Y. Xi, A. Wang, J. Wang, B. Teng, S. Bai, Synergism of surface strain and interfacial polarization on Pd@Au core-shell cocatalysts for highly efficient photocatalytic CO_2 reduction over TiO_2, J. Mater. Chem. A 8 (2020) 7350–7359.

[13] Y. Lia, W.N. Wang, Z. Zhan, M.H. Woo, C.Y. Wu, P. Biswa, Photocatalytic reduction of CO_2 with H_2O on mesoporous silica supported Cu/TiO_2 catalysts, Appl. Catal. B 100 (2010) 386–392.

[14] X. Li, J. Yu, M. Jaroniec, X. Chen, Cocatalysts for selective photoreduction of CO_2 into solar fuels, Chem. Rev. 119.6 (2019) 3962–4179.
[15] L. Zhang, Q. Zheng, Y. Xie, Z. Lan, O.V. Prezhdo, W.A. Saidi, J. Zhao, Delocalized impurity phonon induced electron-hole recombination in doped semiconductors, Nano Lett. 18 (2018) 1592–1599.
[16] P. Yue, H. She, L. Zhang, B. Niu, R. Lian, J. Huang, L. Wang, Q. Wang, Super-hydrophilic CoAl-LDH on $BiVO_4$ for enhanced photoelectrochemical water oxidation activity, Appl. Catal. B 286 (2021) 119875.
[17] H.L. Tan, R. Amal, Y.H. Ng, Alternative strategies in improving the photocatalytic and photoelectrochemical activities of visible light-driven $BiVO_4$: a review, J. Mater. Chem. A 5 (2017) 16498–16521.
[18] J. Wu, L. Xiong, Y. Hu, Y. Yang, X. Zhang, T. Wang, Z. Tang, A. Sun, Y. Zhoud, J. Shen, Z. Zou, Organic half-metal derived erythroid-like $BiVO_4$/hm-C_4N_3 Z-Scheme photocatalyst: Reduction sites upgrading and rate-determining step modulation for overall CO_2 and H_2O conversion, Appl. Catal. B 295 (2021) 120277.
[19] C. Zhou, S. Wang, Z. Zhao, Z. Shi, S. Yan, Z. Zou, A facet-dependent schottky- junction Electron shuttle in a $BiVO_4$ {010}-Au-Cu_2O Z-Scheme photocatalyst for efficient charge separation, Adv. Funct. Mater. 28 (2018) 181214.
[20] C. Kim, K.M. Cho, A. Al-Saggaf, I. Gereige, H.T. Jung, Z-scheme photocatalytic CO_2 conversion on three-dimensional $BiVO_4$/Carbon-Coated Cu_2O nanowire arrays under visible light, ACS Catal. 8 (2018) 4170–4177.
[21] Q. Han, L. Li, W. Gao, Y. Shen, L. Wang, Y. Zhang, X. Wang, Q. Shen, Y. Xiong, Y. Zhou, Z. Zou, Elegant construction of $ZnIn_2S_4$/$BiVO_4$ hierarchical heterostructures as Direct Z-scheme photocatalysts for efficient CO_2 photoreduction, ACS Appl. Mater. Interfaces 13 (2021) 15092–15100.
[22] X. Wang, Y. Wang, M. Gao, J. Shen, X. Pu, Z. Zhang, H. Lin, X. Wang, $BiVO_4$ /$Bi_4Ti_3O_{12}$ heterojunction enabling efficient photocatalytic reduction of CO_2 with H_2O to CH_3OH and CO, Appl. Catal. B 270 (2020) 118876.
[23] J. Li, W. Shao, M. Geng, S. Wan, M. Ou, Y. Chen, Combined Schottky junction and doping effect in $Cd_xZn_{1-x}S$@Au/$BiVO_4$ Z-Scheme photocatalyst with boosted carriers charge separation for CO_2 reduction by H_2O, J. Colloid Interface Sci. 606 (2022) 1469–1476.
[24] L. Huang, Z. Duan, Y. Song, Q. Li, L. Chen, $BiVO_4$ microplates with oxygen vacancies decorated with metallic Cu and Bi nanoparticles for CO_2 photoreduction, ACS Appl. Nano Mater. 4 (2021) 3576–3585.
[25] J.F. deBrito, P.G. Corradini, M.V.B. Zanoni, F. Marken, L.H. Mascaro, The influence of metallic Bi in $BiVO_4$ semiconductor for artificial photosynthesis, J. Alloys Compd. 851 (2021) 156912.
[26] Z. Duan, X. Zhao, C. Wei, L. Chen, Ag-Bi/$BiVO_4$ chain-like hollow microstructures with enhanced photocatalytic activity for CO_2 conversion, Appl. Catal. A 594 (2020) 117459.
[27] Z. Zhu, C.X. Yang, Y.T. Hwang, Y.C. Lin, R.J. Wu, Fuel generation through photoreduction of CO_2 on novel Cu/$BiVO_4$, Mater. Res. Bull. 130 (2020) 110955.
[28] K. Wang, L. Zhang, Y. Su, S. Sun, Q. Wang, H. Wang, W. Wang, Boosted CO_2 photoreduction to methane via Co doping in bismuth vanadate atomic layers, Catal. Sci. Technol. 8 (2018) 3115–3122.

[29] S. Gao, B. Gu, X. Jiao, Y. Sun, X. Zu, F. Yang, W. Zhu, C. Wang, Z. Feng, B. Ye, Y. Xie, Highly efficient and exceptionally durable CO_2 photoreduction to methanol over freestanding defective single-unit-cell bismuth vanadate layers, J. Am. Chem. Soc. 139 (2017) 3438–3445.
[30] J. Xiong, J. Di, J. Xia, W. Zhu, H. Li, Surface defect engineering in 2D nanomaterials for photocatalysis, Adv. Funct. Mater. 28 (2018) 1801983.
[31] L. Ran, J. Hou, S. Cao, Z. Li, Y. Zhang, Y. Wu, B. Zhang, P. Zhai, L. Sun, Defect engineering of photocatalysts for solar energy conversion, Sol. RRL 4 (2020) 1900487.
[32] Y. Huang, Y. Yu, Y. Yu, B. Zhang, Oxygen vacancy engineering in photocatalysis, Sol. RRL 4 (2020) 2000037.
[33] K. Edalati, Z. Horita, A review on high-pressure torsion (HPT) from 1935 to 1988, Mater. Sci. Eng. A 652 (2016) 325–352.
[34] K. Edalati, Review on recent advancements in severe plastic deformation of oxides by high-pressure torsion (HPT), Adv. Eng. Mater. 21 (2019) 1800272.
[35] K. Edalati, A. Bachmaier, V.A. Beloshenko, Y. Beygelzimer, V.D. Blank, W.J. Botta, K. Bryła, J. Čížek, S. Divinski, N.A. Enikeev, Y. Estrin, G. Faraji, R.B. Figueiredo, M. Fuji, T. Furuta, T. Grosdidier, J. Gubicza, A. Hohenwarter, Z. Horita, J. Huot, Y. Ikoma, M. Janeček, M. Kawasaki, P. Král, S. Kuramoto, T.G. Langdon, D.R. Leiva, V.I. Levitas, A. Mazilkin, M. Mito, H. Miyamoto, T. Nishizaki, R. Pippan, V.V. Popov, E.N. Popova, G. Purcek, O. Renk, Á. Révész, X. Sauvage, V. Sklenicka, W. Skrotzki, B.B. Straumal, S. Suwas, L.S. Toth, N. Tsuji, R.Z. Valiev, G. Wilde, M.J. Zehetbauer, X. Zhu, Nanomaterials by severe plastic deformation: review of historical developments and recent advances, Mater. Res. Lett. 10 (2022) 163–256.
[36] K. Edalati, R. Uehiro, S. Takechi, Q. Wang, M. Arita, M. Watanabe, T. Ishihara, Z. Horita, Enhanced photocatalytic hydrogen production on GaN-ZnO oxynitride by introduction of strain-induced nitrogen vacancy complexes, Acta Mater. 185 (2020) 149–156.
[37] R.P.I. Halder, C.N.J. Wagner, X-Ray diffraction study of the effects of solutes on the occurrence of stacking faults in silver-base alloys, J. Appl. Phys. 33 (1962) 3451–3458.
[38] J. Chastain, Handbook of X-ray Photoelectron Spectroscopy, Perkin-Elmer Corporation, Eden Prairie, MN, USA, 1992.
[39] S. Akrami, M. Watanabe, T.H. Ling, T. Ishihara, M. Arita, M. Fuji, K. Edalati, High pressure TiO_2-II polymorph as an active photocatalyst for CO_2 to CO conversion, Appl. Catal. B 298 (2021) 120566.
[40] S. Akrami, Y. Murakami, M. Watanabe, T. Ishihara, M. Arita, M. Fuji, K. Edalati, Defective high-entropy oxide photocatalyst with high activity for CO_2 conversion, Appl. Catal. B 303 (2022) 120896.
[41] Z. Zhang, F. Zhou, E.J. Lavernia, On the analysis of grain size in bulk nanocrystalline materials via x-ray diffraction, Metall. Mater. Trans. 34 (2003) 1349–1355.
[42] Q. Luo, L. Zhang, X. Chen, O.K. Tan, K.C. Leong, Mechanochemically synthesized m-$BiVO_4$ nanoparticles for visible light photocatalysis, RSC Adv. 6 (2016) 15796-15802.
[43] K. Nakagawa, M. Hayashi, K. Takano-Satoh, H. Matsunaga, H. Mori, K. Maki, Y. Onuki, S. Suzuki, S. Sato, Characterization of dislocation rearrangement in FCC metals during work hardening using X-ray diffraction line-profile analysis, Quantum Beam Sci. 4 (2020) 36.
[44] J.M. Wu, Y. Chen, L. Pan, P. Wang, Y. Cui, D. Kong, L. Wang, X. Zhang, J.J. Zou, Multi-layer monoclinic $BiVO_4$ with oxygen vacancies and V^{4+} species for highly efficient visible-light photoelectrochemical applications, Appl. Catal. B. 221 (2018) 187–195.

[45] P. Stathi, M. Solakidou, Y. Deligiannakis, Lattice defects engineering in W-, Zr-doped $BiVO_4$ by flame spray pyrolysis: enhancing photocatalytic O_2 evolution, Nanomaterials 11 (2021) 501.
[46] J. Xu, Z. Bian, X. Xin, A. Chen, H. Wang, Size dependence of nanosheet $BiVO_4$ with oxygen vacancies and exposed {0 0 1} facets on the photodegradation of oxytetracycline, Chem. Eng. J. 337 (2018) 684–696.
[47] M. Guo, Y. Wang, Q. He, W. Wang, W. Wang, Z. Fua, H. Wang, Enhanced photocatalytic activity of S-doped $BiVO_4$ photocatalysts, RSC Adv. 5 (2015) 58633–58639.
[48] X. Yuan, X. Sun, H. Zhou, S. Zeng, B. Liu, X. Li, D. Liu, Free-standing electrospun W-doped $BiVO_4$ porous nanotubes for the efficient photoelectrochemical water oxidation, Front. Chem.8 (2020) 311.
[49] Q. Pan, K. Yang, G. Wang, D. Li, J. Sun, B, Yang, Z. Zou, W. Hu, K. Wen, H. Yang, $BiVO_4$ nanocrystals with controllable oxygen vacancies induced by Zn-doping coupled with graphene quantum dots for enhanced photoelectrochemical water splitting, Chem. Eng. J. 372 (2019) 399–407.
[50] J.A. Weil, J.R. Bolton, Electron Paramagnetic Resonance: Elementary Theory and Practical Applications, John Wiley & Sons, 2007.
[51] A. Schweiger, G. Jeschke, Principles of Pulse Electron Paramagnetic Resonance, Oxford University Press on Demand, 2001.
[52] W. Qiu, S. Xiao, J. Ke, Z. Wang, S. Tang, K. Zhang, W. Qian, Y. Huang, D. Huang, Y. Tong, S. Yang, Freeing the polarons to facilitate charge transport in $BiVO_4$ from oxygen vacancies with an oxidative 2D precursor, Angew. Chem. 131 (2019) 19263–19271.
[53] B. Oberdorfer, B. Lorenzoni, K. Unger, W. Sprengel, M. Zehetbauer, R. Pippan, R. Wurschum, Absolute concentration of free volume-type defects in ultrafine-grained Fe prepared by high-pressure torsion, Scr. Mater. 63 (2010) 452–455.
[54] J. Čížek, M. Janeček, T. Vlasák, B. Smola, O. Melikhova, R.K. Islamgaliev, S.V. Dobatkin, The development of vacancies during severe plastic deformation, Mater. Trans. 60 (2019) 1533–1542.
[55] W.J. Chun, A. Ishikawa, H. Fujisawa, T. Takata, J.N. Kondo, M. Hara, M. Kawai, Y. Matsumoto, K. Domen, Conduction and valence band positions of Ta_2O_5, TaON, and Ta_3N_5 by UPS and electrochemical methods, J. Phys. Chem. B 107 (2003) 1798–1803.
[56] Y. Hermans, S. Murcia-López, A. Klein, R. van de Krol, T. Andreu, J.R. Morante, T. Toupance, W. Jaegermann, Analysis of the interfacial characteristics of $BiVO_4$/metal oxide heterostructures and its implication on their junction properties, Phys. Chem. Chem. Phys. 21 (2019) 5086–5096.
[57] H.L. Tan, X. Wen, R. Amal, Y.H. Ng, $BiVO_4$ {010} and {110} relative exposure extent: governing factor of surface charge population and photocatalytic activity, J. Phys. Chem. Lett. 7 (2016) 1400–1405.
[58] M.C. Wu, C.H. Chen, W.K. Huang, K.C. Hsiao, T.H. Lin, S.H. Chan, P.Y. Wu, C.F. Lu, Y.H. Chang, T.F. Lin, K.H. Hsu, J.F. Hsu, K.M. Lee, J.J. Shyue, K. Kordás, W.F. Su, Improved solar-driven photocatalytic performance of highly crystalline hydrogenated TiO_2 nanofibers with core-shell structure, Sci. Rep. 7 (2017) 40896.
[59] I. Nakamura, N. Negishi, S. Kutsuna, T. Ihara, S. Sugihara, K.J. Takeuchi, Role of oxygen vacancy in the plasma-treated TiO_2 photocatalyst with visible light activity for NO removal, J. Mol. Catal. A 161 (2000) 205–212.

[60] J. Li, M. Zhang, Z. Guan, Q. Li, C. He, J. Yang, Synergistic effect of surface and bulk single-electron-trapped oxygen vacancy of TiO_2 in the photocatalytic reduction of CO_2, Appl. Catal. B 206 (2017) 300–307.
[61] Z.F. Huang, L. Pan, J.J. Zou, X. Zhang, L. Wang, Nanostructured bismuth vanadate-based materials for solar-energy-driven water oxidation: a review on recent progress, Nanoscale 6 (2014) 14044–14063.
[62] F.S. Hegner, D. Forrer, J.R. Galán-Mascarós, N. López, A. Selloni, Versatile nature of oxygen vacancies in bismuth vanadate bulk and (001) surface, J. Phys. Chem. Lett. 10 (2019) 6672–6678.
[63] D.K. Lee, K.S. Choi, Enhancing long-term photostability of $BiVO_4$ photoanodes for solar water splitting by tuning electrolyte composition, Nat. Energy 3 (2018) 53-60.
[64] F.M. Toma, J.K. Cooper, V. Kunzelmann, M.T. McDowell, J. Yu, D.M. Larson, N.J. Borys, C. Abelyan, J.W. Beeman, K.M. Yu, J. Yang, L. Chen, M.R. Shaner, J. Spurgeon, F.A. Houle, K.A. Persson, I.D. Sharp, Mechanistic insights into chemical and photochemical transformations of bismuth vanadate photoanodes, Nat. Commun. 7 (2016) 12012.
[65] Z. Miao, G. Wang, X. Zhang, X. Dong, Oxygen vacancies modified TiO_2/Ti_3C_2 derived from MXenes for enhanced photocatalytic degradation of organic pollutants: the crucial role of oxygen vacancy to schottky junction, Appl. Surf. Sci. 528 (2020) 146929.
[66] X. Liang, G. Wang, X. Dong, G. Wang, H. Ma, X. Zhang, Graphitic carbon nitride with carbon vacancies for photocatalytic degradation of bisphenol A, ACS Appl. Nano Mater. 2 (2019) 517–524.
[67] G. Wang, Y. Zhao, H. Ma, C. Zhang, X. Dong, X. Zhang, Enhanced peroxymonosulfate activation on dual active sites of N vacancy modified g-C_3N_4 under visible-light assistance and its selective removal of organic pollutants, Sci. Total Environ. 756 (2021) 144139.
[68] G. Silversmit, D. Depla, H. Poelman, G.B. Marin, R. De Gryse, Determination of the V2p XPS binding energies for different vanadium oxidation states (V^{5+} to V^{0+}), J. Electron Spectrosc. Relat. Phenom. 135 (2004) 167–175.
[69] Y. Park, K. J. McDonald and K. S. Choi, Progress in bismuth vanadate photoanodes for use in solar water oxidation, Chem. Soc. Rev. 42 (2013) 2321–2337.
[70] Y. Zhang, Y. Guo, H. Duan, H. Li, C. Sun, H. Liu, Facile synthesis of V^{4+} self-doped, [010] oriented $BiVO_4$ nanorods with highly efficient visible light-induced photocatalytic activity, Phys. Chem. Chem. Phys. 16 (2014) 24519–24526.
[71] S. Akrami, P. Edalati, M. Fuji, K. Edalati, High-entropy ceramics: review of principles, production and applications, Mater. Sci. Eng. R 146 (2021) 100644.